ACS Photonics

pubs.acs.org/journal/apchd5

Article

Topology with Memory in Nonlinear Driven-Dissipative Photonic Lattices

Subhaskar Mandal,* Gui-Geng Liu, and Baile Zhang*

Cite This: *ACS Photonics* 2023, 10, 147−154

Read Online

ACCESS | Metrics & More | Article Recommendations | Supporting Information

ABSTRACT: We consider a photonic lattice of nonlinear lossy resonators subjected to a coherent drive, where the system remembers its topological phase. Initially, the system is topologically trivial. After the application of an additional coherent pulse, the intensity is increased, which modifies the couplings in the system and then induces a topological phase transition. However, when the effect of the pulse dies out, the system does not go back to the trivial phase. Instead, it remembers the topological phase and maintains its topology acquired during the pulse application. The pulse can be used as a switch to trigger amplification of the topological modes. We further show that the amplification takes place at a different frequency as well as at a different position from those of the pulse, indicating frequency conversion and intensity transfer. Our work can be useful in triggering the different functionalities of active topological photonic devices.

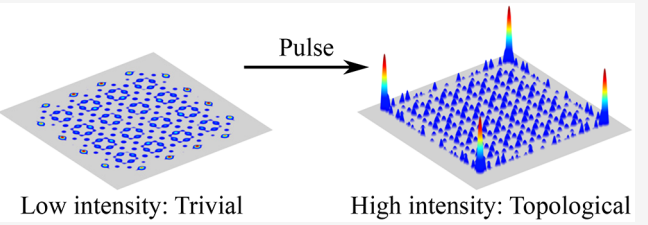

KEYWORDS: *nonlinear topology, topological corner modes, bistability, optical memory, topological laser*

INTRODUCTION

The intriguing properties of topological photonics have enabled widespread applications in modern optical devices, such as robust signal transport,[1−5] optical delay line,[6] quantum interface,[7] quantum light source,[8] robust splitters,[9] and topological lasers.[10−14] Topological photonics is also promising for optical information processing technologies. For example, valley photonic crystals are identified as an excellent candidate for robust information transfer in next-generation devices.[3−5] Similar to transferring the information, the ability to store it in memory is an equally important task in information processing. However, optical memories along with topological protection have not been explored until now.

Nonlinearity is at the core of memory devices. The interplay between the nonlinearity and the topology has made way for many novel effects such as topological solitons,[15−19] high harmonic generation,[20,21] topological phase transitions,[22−27] and others[28−33] (see ref 34 for a comprehensive review). However, none of the previous works can show the memory feature: once the key ingredient, which induces the functionalities, is removed from the scheme, the systems can no longer continue to exhibit such effects.

In this work, we introduce for the first time a topological phase with memory in a lattice of lossy resonators having local onsite Kerr nonlinearity, where the system remembers its topological phase. The lossy nature of the system leads to a steady state in the presence of a coherent drive F. However, due to the nonlinearity, our system subjected to a properly designed F shows not only one but two steady states: low- and high-intensity states. Our system is topologically trivial, and after F is introduced, it attains the low-intensity steady state. The introduction of an additional coherent pulse increases the intensity of the system. At higher intensities, the nonlinear interaction modifies the couplings, and the otherwise-trivial system becomes topological. However, at longer times when the effect of the pulse dies, the system does not go back to its previous trivial phase. Instead, it remembers the topological phase and maintains its topology acquired during the pulse application. As an application of this effect, we show a unique amplification phenomenon, where the amplification is triggered by a pulse.

We start by considering a nonlinear optical resonator subjected to a coherent drive F (see Figure 1a), which is represented by the following nonlinear Schrödinger equation (NLSE):

$$i\frac{\partial\psi}{\partial t} = (\omega_0 - i\Gamma)\psi + |\psi|^2\psi + F\exp(-i\omega_p t) \quad (1)$$

Here ω_0 is the onsite potential, and Γ is the linear decay. The next term represents the defocusing Kerr nonlinearity, where the nonlinear coefficient is set to 1. F is a coherent drive having

Received: September 1, 2022
Published: January 6, 2023

https://doi.org/10.1021/acsphotonics.2c01367
ACS Photonics 2023, 10, 147−154

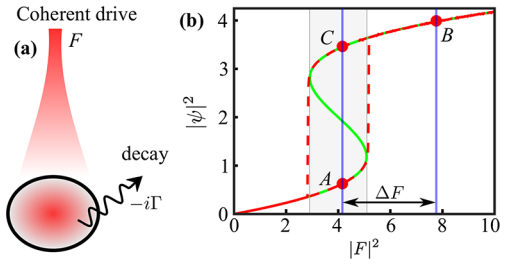

Figure 1. (a) Schematic of a coherently driven nonlinear resonator. (b) Analytically and numerically calculated bistable curves in green and red, respectively. Parameters: $\Delta = -3$, $\Gamma = 1$.

frequency ω_p. For the steady-state ψ_s, where $\partial\psi_s/\partial t = 0$, one can obtain

$$|F|^2 = [(\Delta + |\psi_s|^2)^2 + \Gamma^2]|\psi_s|^2 \tag{2}$$

where $\Delta = (\omega_0 - \omega_p)$. From eq 2, it is easy to find that within the gray region for each $|F|^2$ three possible $|\psi_s|^2$ exist (see Figure 1b). However, in practice, the middle branch is not stable. This can be confirmed by numerically solving eq 1, but letting F vary very slowly in time such that at each time step steady state can be reached (more details on the numerical calculation of bistability can be found in the Supporting Information). The red dashed curve obtained numerically follows the analytical green curve; however, the middle branch does not appear. Consequently, the system shows bistability by allowing both the low- and high-intensity stable states for a fixed value of F within the gray region. The absence of the middle branch of the bistability curve can be explained using the stability analysis based on the first Lyapunov criterion[35] (see the Supporting Information).

An important characteristic of bistability is their ability to mimic the memory: the state of the system is determined not only by the current parameters (such as F) but also by its previous state. For example, let us consider a system that is initially in the low-intensity state "A" as shown in Figure 1b. An additional coherent drive ΔF is added such that the system moves to a high-intensity state "B". Now if ΔF is removed, the system does not return back to its original state "A"; instead, it chooses the high-intensity state "C". While determining the final state, the system memorizes the information (high-intensity) about the intermediate state "B", and in the case where "B" is a low-intensity state, the system would return to the original state "A" upon removing ΔF.

MODEL

We arrange the nonlinear resonators in a 2D lattice. In order to be close with experiments, we model the dynamics of the system using the NLSE in the continuum limit (where the space is taken as continuous). Without the loss of generality, we work with the dimensionless NLSE, which is expressed as

$$\begin{aligned} i\frac{\partial\psi(x,y)}{\partial t} &= [-\nabla^2 + V(x,y) - i\Gamma]\psi(x,y) \\ &\quad + |\psi(x,y)|^2\psi(x,y) + F(x,y)e^{-i\omega_p t} \\ &\quad + F_p(x,y)\exp\left[-\frac{(t-t_0)^2}{2\tau^2}\right]e^{-i\omega_p t} \end{aligned} \tag{3}$$

Here $\nabla^2 \equiv (\partial^2/\partial x^2 + \partial^2/\partial y^2)$ is the transverse Laplacian operator, V is the external potential profile corresponding to the resonators, Γ is the linear decay, F is a position-dependent coherent pump having frequency ω_p, and F_p is a coherent pulse having duration τ centered at time t_0. Next, we consider circular resonators having diameter d_m, which we call *main* resonators. Two *main* resonators separated by L are coupled via an *auxiliary* larger resonator having diameter d_a, where $d_a > d_m$ (see Figure 2a). The potential is taken as $V = 0$ inside and $V = V_0 > 0$ outside the resonators.

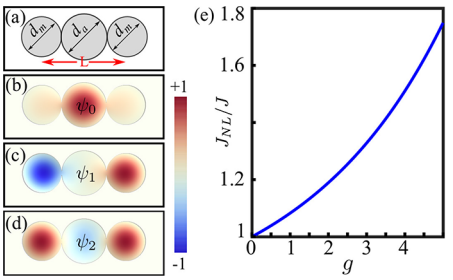

Figure 2. (a) Schematic of two *main* resonators connected by an *auxiliary* resonator. (b, c, d) The lowest three modes of the system shown in (a). (e) The ratio of the coupling in the nonlinear regime J_{NL} to the linear coupling J between two *main* resonators as a function of the intensity of the *auxiliary* resonator. Parameters: $V_0 = 236$, $L = 2.13$, $d_m = 1$, $d_a = 1.13$.

To capture the role of nonlinearity, we first consider two *main* resonators connected by an *auxiliary* resonator as shown in Figure 2a. The ground-state wave function ψ_0 is mainly localized at the *auxiliary* resonator (see Figure 2b), whereas the first (ψ_1) and second (ψ_2) excited states are localized at the *main* resonators (see Figure 2c,d). The coupling strength J between the *main* resonators can be estimated from the difference in the eigenvalues of the symmetric (E_2) and asymmetric (E_1) eigenstates, where $J = (E_2 - E_1)/2$. The important feature that plays a key role and signifies the nonlinear effect in this work is the ability to control the coupling between the *main* resonators by changing the intensity of the *auxiliary* resonator. This is captured by choosing an effective potential $V_{\text{eff}} = V + g|\psi_0|^2$, where g corresponds to the peak value of the ground-state intensity, and obtaining the coupling in the nonlinear regime J_{NL} in a self-consistent way. Figure 2e shows the enhancement of J_{NL} compared to J as a function of g. However, such an enhancement of J_{NL} is limited. Once g becomes larger than the difference between the fundamental frequencies of the *main* and the *auxiliary* resonators, J_{NL} would start to decrease and for $g \to \infty$, $J_{NL} \to 0$.

TOPOLOGICAL MEMORY

Now that we have all the ingredients, we proceed to study the topological phase in a 2D square lattice formed by the above-mentioned resonators, where between any two *main* resonators there is an *auxiliary* resonator. Recalling that the intensity of the *auxiliary* resonators enhances the coupling between the *main* resonators, we choose the coherent pump profile in such a way that the intercells are coupled strongly similar to the 2D Su–Schrieffer–Heeger (SSH) model.[36] The spatial profile of the coherent pump is expressed as

$$F(x,y) = P_0 \sum_{X_n,Y_n} \exp\left[-\frac{(x-X_n)^2 + (y-Y_n)^2}{2\sigma^2}\right] \tag{4}$$

https://doi.org/10.1021/acsphotonics.2c01367
ACS Photonics 2023, 10, 147−154

where P_0 is the strength of the pump and $\{X_n, Y_n\}$ are the coordinates of the center of the pumped *auxiliary* resonators as shown in Figure 3a. Such pump profiles are readily achieved in

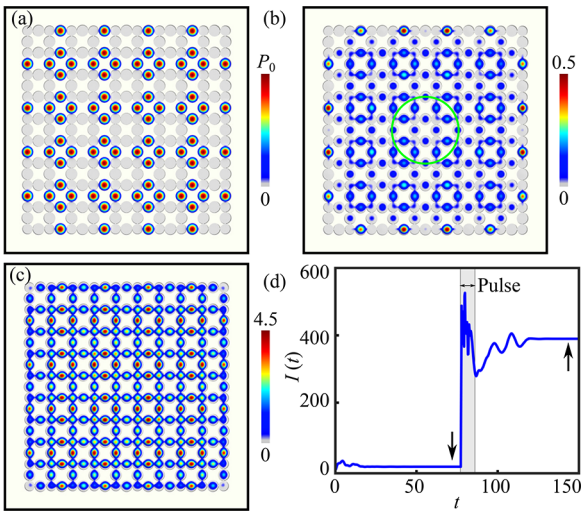

Figure 3. (a) Spatial profile of the coherent pump. (b, c) Steady states of the system before and after the coherent pulse F_p, respectively. The green circle in (b) represents the width of F_p. (d) The total intensity of the system as a function of time showing the bistable behavior. The two arrows indicate the times at which the states in (b, c) are plotted. Parameters: $\Gamma = 0.13$, $P_0 = \sqrt{0.5}$, $\omega_p = 14.74$, $\sigma = 0.3$, $\tau = 23.9$, $t_0 = 77$. F_p is a Gaussian pulse having strength $20P_0$ and width 7.5σ. All other parameters are kept the same as those in Figure 2.

practice using the spatial light modulators.[37,38] We choose the value of P_0 such that the *auxiliary* resonators subjected to the pump are bistable. To show the bistable behavior of the whole system, we solve eq 3 without the pulse ($F_p = 0$) and take zeros as the initial condition. While plotting the spatial profiles, we keep the background potential to distinguish the intensities between the *main* and *auxiliary* resonators. Figure 3b shows the steady state of the system before the application of the pulse, where intensity is mainly localized at the pumped *auxiliary* resonators. The coupling between the resonators results in slightly nonidentical bistability curves of the resonators placed at different positions (see Supporting Information). Due to this, the intensity among the pumped resonators varies a little, but they remain in the low-intensity state, where $|\psi|^2$ is negligible.

Next, we apply a Gaussian-shaped coherent pulse F_p centered at the bulk as shown by the green circle in Figure 3b. The addition and removal of the additional pump ΔF in Figure 1b is performed by the pulse F_p here. In Figure 3c the steady state of the system after the application of the pulse is shown. The system indeed remembers the high intensity created by the pulse, and once the effect of the pulse dies out, the system chooses to stay at the high-intensity state. Compared to the low-intensity state in Figure 3b, a much larger intensity outside the pumped *auxiliary* resonators exists, which signifies the enhancement of the coupling due to significant $|\psi|^2$. In Figure 3d the total intensity of the system, $I(t) = \int \psi(x, y, t)\, dx\, dy$, where the integration is over the whole system, is shown as a function of time, which shows the bistable behavior of the system. The full dynamics of the system is shown in Movie 1.

We have performed all the calculations corresponding to the 2D lattice on a $2^9 \times 2^9$ grid. The Laplacian is taken into account through the FFT (fast Fourier transform) spectral method. It should be noted that the finite difference (FD) method can also be implemented to express the Laplacian. However, FD requires larger computational memory and is more time-consuming compared to the FFT method. The time dynamics is performed using Matlab's ODE solvers, which relies on well-established numerical techniques, such as the explicit Runge−Kutta (4,5) formula, the Dormand−Prince pair.[39]

Having established the memory effect in the 2D lattice, here we show the topology associated with it. In Figure 4a the

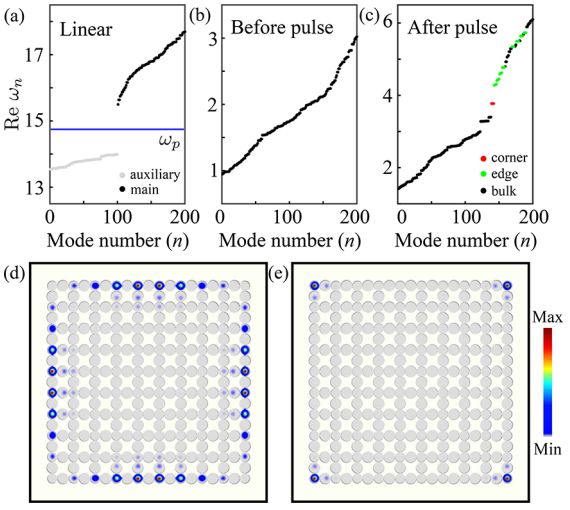

Figure 4. (a, b, c) Real eigenfrequencies for different cases. In (a) the *auxiliary* resonator band is shown in gray and the *main* resonator band is shown in black. Red and green dots in (c) correspond to the corner and edge modes, respectively. The blue line in (a) represents ω_p, with respect to which (b, c) are rescaled. (d, e) Spatial profiles of an edge and a corner mode, respectively. All the parameters are kept the same as those in Figure 3.

eigenfrequencies of the linear system are shown, which can be found by putting the nonlinear and pumping terms to zero in eq 3 and diagonalizing its corresponding Hamiltonian. The lower band (shown in gray) has the main contributions from to the *auxiliary* resonators, whereas the upper band has the main contributions from the *main* resonators. For the rest of the work, we shall focus on the *main* resonator band, which is topologically trivial and gapless in the linear regime. To include the nonlinear effect, we study the Bogoliubov fluctuations on top of the steady state:[40]

$$\psi(x, y) = \psi_s(x, y) + u_n(x, y)e^{-i\omega_n t} + v_n^*(x, y)e^{i\omega_n^* t} \quad (5)$$

Here ψ_s represent the low- and high-intensity steady states shown in Figure 3b,c, respectively. u_n and v_n represent the fluctuations having frequency ω_n. Substituting eq 5 into eq 3 and by ignoring the higher-order terms in u_n and v_n, we obtain the following eigenvalue equation:

$$\begin{bmatrix} H_0 + 2|\psi_s|^2 & \psi_s^2 \\ -\psi_s^{2*} & -H_0^* - 2|\psi_s|^2 \end{bmatrix} \begin{bmatrix} u_n \\ v_n \end{bmatrix} = \omega_n \begin{bmatrix} u_n \\ v_n \end{bmatrix} \quad (6)$$

https://doi.org/10.1021/acsphotonics.2c01367
ACS Photonics 2023, 10, 147−154

where $H_0 = [-\nabla^2 + V(x, y) - i\Gamma - \omega_p]$, which is rescaled with respect to the pump frequency ω_p.

The fluctuation Hamiltonian has particle-hole symmetry, which makes the eigenfrequencies appear in pairs $(\omega_n, -\omega_n^*)$. The Hilbert space of the fluctuation Hamiltonian is double in size compared to the linear one. Consequently, for better visualization we show the eigenfrequencies near the *main* resonator band and for Re $\omega_n > 0$. Figure 4b shows the eigenfrequencies of the fluctuations before the pulse is applied. Similar to the linear case, the band is gapless. This is understandable, as for the low-intensity state, $|\psi|^2$ is not significant enough to induce the topological transition. After the application of the pulse positioned at the bulk, the system switches to the high-intensity state. In this case, the nonlinear effect becomes significant and the coupling between the *main* resonators connected by a pumped *auxiliary* resonator increases. The system goes through a topological phase transition from trivial to second-order topological phase, where a bulk band gap opens and four topological corner modes appear. An effective tight-binding model based on the strong coupling induced by the pump can reproduce the topological corner modes (see the Supporting Information).

In Figure 4c the eigenfrequencies of the fluctuation after the application of the pulse are shown, where the topological corner modes are marked in red and the edge modes are shown in green. Figure 4d,e show the spatial profiles of one of the topological edge modes ($n = 146$) and topological corner modes ($n = 142$), respectively. In experiment, the topological modes will be hidden in the high-intensity steady state. However, they can be probed using a weak additional coherent pump followed by the frequency filtration to subtract the steady state.

Higher-order topological phases have been an intense area of research.[36,41,42] We note that the effect of the on-site Kerr nonlinearity on these system has been studied recently.[30,32,33,43] However, the previous works consider the effect of nonlinearity on the already existing linear topological band structure. The presented result is the first example where on-site Kerr nonlinearity alone induces higher-order topological phase transition. Although here we have focused on the topological corner modes, it would be interesting to investigate further whether different truncations can lead to different types of edge states, such as the ones shown in ref 44.

CALCULATION OF THE TOPOLOGICAL INVARIANT

Here we calculate the bulk polarization, which characterizes the topological corner modes,[45] using a biorthogonal Wilson loop.[46] We define a Wilson line along the y-direction as

$$\Xi_y^{m,n}(k_x, k_y) = \langle \Psi^{L,m}_{k_x,k_y+\Delta_y} | \Psi^{R,n}_{k_x,k_y} \rangle = \int_{\text{unitcell}} \Psi^{L,m*}_{k_x,k_y+\Delta_y}(x, y) \Psi^{R,n}_{k_x,k_y}(x, y)\, dx\, dy \tag{7}$$

where $\Psi^n_{k_x, k_y}$ represents the Bloch eigenvectors of the fluctuations (see Supporting Information for details on the Bloch eigenvector calculation), and L and R correspond to the left and right Bloch eigenstates, respectively. $\Delta_y = 2\pi/N_y$, where N_y is the total number of points used along the y-direction of the Brillouin zone for calculation. Taking the periodicity as one, the Wilson loop along the y-direction is defined as

$$W^y(k_x, k_y) = \Xi_y^{m,n}(k_x, k_y + 2\pi)\ldots\Xi_y^{m,n}(k_x, k_y + 2\Delta_y) \times \Xi_y^{m,n}(k_x, k_y + \Delta_y)\Xi_y^{m,n}(k_x, k_y) \tag{8}$$

The Wannier Hamiltonian is given by

$$H_W^y(k_x, k_y) = -\frac{i}{2\pi}\log[W^y(k_x, k_y)] \tag{9}$$

The eigenvalues of H_W^y form the Wannier bands, which are shown in Figure 5. The bulk polarization $P = (P_x, P_y)$ is the same as the Wannier center. For a topologically trivial system $P = (0, 0)$. The x component of the bulk polarization P_x is given by summing all the eigenvalues ν_y corresponding to all the momenta k_x.[45] It can be seen from Figure 5 that $P_x \approx 0.5$. Since the system has C_4 rotational symmetry, one can obtain a similar result by choosing the Wilson loop along the x-direction, such that the y component of the bulk polarization $P_y \approx 0.5$ and the total polarization becomes $P \approx (0.5, 0.5)$, making the system topologically nontrivial.

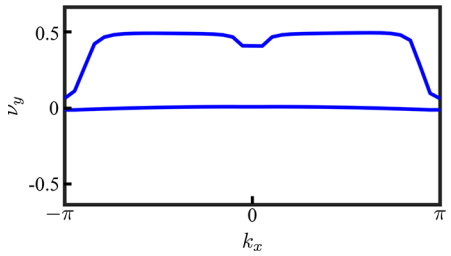

Figure 5. Plot of the Wannier bands obtained by diagonalizing eq 9.

AMPLIFICATION OF THE CORNER MODES

As an application, we use our proposed scheme to control the functionality of an active topological photonic device. We introduce gain at the *main* four corner resonators of the 2D lattice. The gain is modeled by adding a term $+iG(x, y)\psi(x, y)$ at the right-hand side of eq 3, where $G(x, y)$ is composed of four Gaussians centered at the four corners having width σ and peak value G_0. In this case, H_0 in eq 6 is updated to $H_0 \rightarrow H_0 + iG(x, y)$. To signify the role of nonlinearity, it is important that the gain alone cannot induce lasing in the linear regime. Consequently, we obtain the complex eigenfrequencies for the linear system. The system stays below the lasing threshold Im $\omega_n < 0$ (see Figure 6a). Next, we take the steady states corresponding to Figure 3b,c and obtain the same plot for the fluctuations before and after the pulse is applied. Similar to the linear case, the modes have Im $\omega_n < 0$ before the application of the pulse (see Figure 6b). However, after the pulse is applied topological corner modes appear, and due to the significant overlap with the gain, only they have Im $\omega_n > 0$, while all other modes remain at Im $\omega_n < 0$ (see Figure 6c). This has a significant effect on the steady states. As predicted from the complex eigenfrequencies, the gain at the four corners does not alter the steady state before the pulse, which is the same as the one obtained without the gain in Figure 3b. However, after the pulse is applied, a large intensity at the corners is observed along with the high-intensity steady state at the bulk (see Movie 2).

To confirm that the intensity at the corners corresponds to the topological corner modes, we further obtain their spatial profile from the time dynamics, which does not rely on the linear Bogoliubov theory (which does not include the higher-

https://doi.org/10.1021/acsphotonics.2c01367
ACS Photonics 2023, 10, 147−154

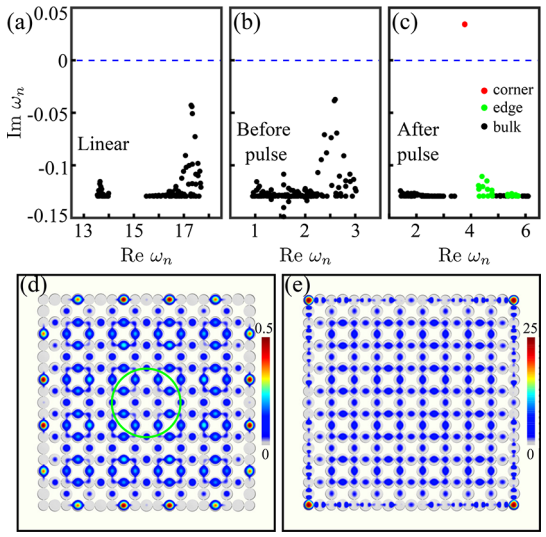

Figure 6. (a, b, c) Complex eigenfrequencies for different cases. Steady states from Figure 3b,c are used for obtaining (b, c). (d, e) Steady states of the system with gain at the corners before and after the pulse is applied, respectively. The green circle in (d) shows the position and width of the pulse. Parameters: Peak value of the gain $G_0 = 3\Gamma$. All other parameters are kept the same as those in Figure 3.

order terms in u and v). We store the solutions at the intermediate time steps corresponding to the steady states in Figure 6d,e and then Fourier transform them along the time axis to move to the frequency dimension. At this stage, we can plot the intensity as a function of frequency. In order to obtain the spatial profile corresponding to a particular frequency, we first multiply with a Gaussian to filter the desired frequency and plot the intensity. In Figure 7a, the above-mentioned steps are given. In Figure 7b,c,d,e the frequency-dependent intensities are shown for different cases. Without the gain, we obtain a peak at the pumped frequency ω_p for both before and after the application of the pulse. It is important to note that no other peak is observed. Now we move on to the case where we introduce gain at the four corners. In this case also, before the application of the pulse a single peak at ω_p is obtained. However, after the pulse is applied a new peak along with the pumped peak is obtained (see Figure 7e). It proves that the amplification at a different frequency has taken place after the application of the pulse. To prove that the amplified modes are the corner modes, we plot the spatial profile of the wave function around the amplified frequency by filtering out the desired frequency using the recipe mentioned in Figure 7a. From the spatial profile shown in Figure 7f, it is clear that the amplified modes are indeed the corner modes. Due to the presence of the $|\psi|^2$ term, the corner modes are shifted in frequency from their linear Bogoliubov spectrum, which does not include the higher-order terms in u and v.

There are a few unique features associated with the amplification process presented above. First, the pulse is positioned away from the corners at the bulk. However, the amplification takes place at the corners of the system, which do not overlap with the pulse. This can be interpreted as the intensity transfer from the bulk to the corner. However, we stress that such a process is completely different from the signal transfer typically associated with the 1D edge modes of first-order topological insulators. Second, the amplified corner states have frequency different from that of the coherent drive, which makes this system suitable for frequency conversion. This is similar to the recent works on the high harmonic generation using topological systems,[20,21,47,48] although here our underlying linear system is topologically trivial. Lastly, the amplification, which is triggered by a pulse, is different from all the previous cases. For example, in lasers if the pumping term (or any other ingredient) that induces amplification (lasing) is removed, understandably the amplification would stop. Due to the memory effect, the functionality in our scheme remains, although the pulse disappears.

We note that a different type of topological memory is proposed recently in dynamic PT-symmetric optical resonators having saturable nonlinearity.[49,50] Unlike the present case, a

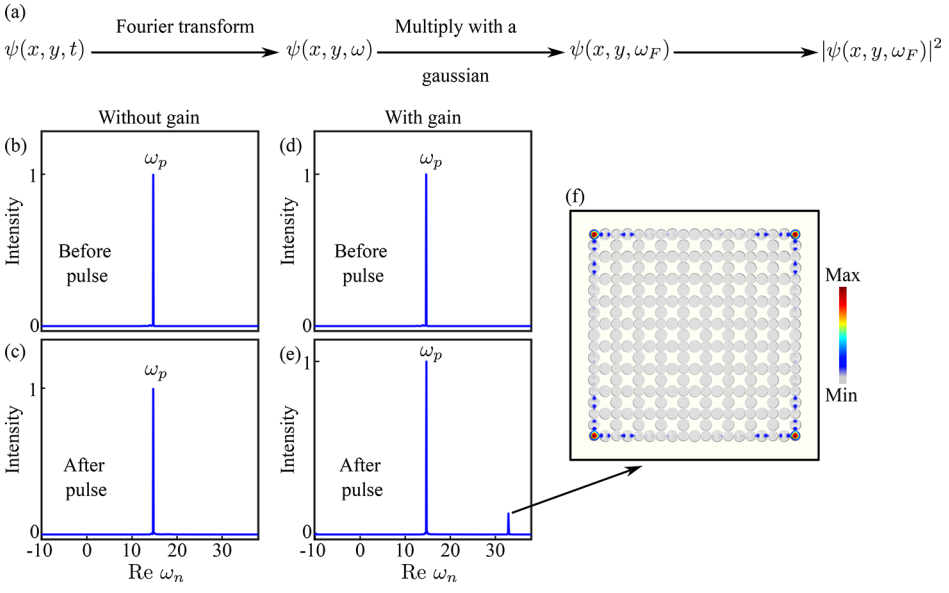

Figure 7. (a) Steps to obtain spatial profiles of ψ at a particular frequency by solving the NLSE. (b, c, d, e) Frequency-dependent intensity. The second peak in (e) corresponds to the amplification. (f) The spatial profile corresponds to the amplification peak in (e), which has the profile of corner modes. In each case we normalize the intensity with respect to the intensity at ω_p.

https://doi.org/10.1021/acsphotonics.2c01367
ACS Photonics 2023, 10, 147−154

lattice is not involved there. Instead, the system consists of a single diatomic or triatomic resonator. The topology introduced in those works is different from the topology associated with band structures in usual topological lattices. There, oscillating quenching states are protected against the defects of the parameter space that preserve dynamical state trajectories.

PROPOSAL FOR EXPERIMENTAL REALIZATION

The NLSE in eq 3 is generally used to describe the topological physics in photonic waveguide arrays.[17,18] Bistability is realized experimentally in waveguide arrays,[51] whereas the Bogoliubov fluctuations in eq 6 can be arranged using the parametric down-conversion.[52−56] Alternatively, the system of exciton−polaritons, where cavity photons exhibit Kerr nonlinearity by coupling strongly with the quantum well excitons, is also a promising platform for realizing our scheme. They are well known for studying topological photonics.[57−64] Bistability is well established for exciton−polaritons.[65−67] Bogoliubov fluctuations naturally arise in polariton systems.[19,68] By choosing the proper physical units, our present parameters can be related to the exciton−polariton lattices.

Here we provide the physical parameters based on the exciton−polariton system. Typically, the system of exciton−polaritons is expressed using the NLSE (also known as the nonlinear Gross−Pitaevskii equation):[69]

$$i\hbar\frac{\partial\phi(X,Y)}{\partial T} = \left[-\frac{\hbar^2}{2m}\left(\frac{\partial^2}{\partial X^2}+\frac{\partial^2}{\partial Y^2}\right)+V_e(X,Y)-i\frac{\hbar}{2\lambda} + \alpha|\phi(X,Y)|^2\right]\phi(X,Y)+f(X,Y) \times \exp(-i\Omega_p t) \tag{10}$$

We restrict ourselves to the bottom of the lower polariton dispersion, where the dispersion can be approximated to be a parabola having effective mass m. V_e is the external potential for the polaritons, which consists of microcavity pillars.[59,70,71] λ is the effective lifetime of the polaritons, which can be controlled by adjusting the quality factor of the cavity. $\alpha > 0$ is the effective polariton−polariton interaction coefficient, which is typically repulsive in nature. f is the coherent drive. Next, we perform the following transformation in order to transform to eq 3:

$$X \to xa,\ Y \to ya,\ V_e \to V\varepsilon_u,\ T \to tt_u,\ \Omega_p \to \omega_p/t_u,\ \lambda \to 2t_u/\Gamma,\ \phi \to \psi\sqrt{\frac{\varepsilon_u}{\alpha}},\ \text{and}\ f \to F\frac{\varepsilon_u^{3/2}}{\sqrt{\alpha}} \tag{11}$$

where x, y, V, Γ, ψ, and F are the dimensionless quantities used in eq 3. Here a is the length unit, $\varepsilon_u = \hbar^2/2ma^2$ is the energy unit, $t_u = 2ma^2/\hbar$ is the time unit, $\sqrt{\varepsilon_u/\alpha}$ is the wave function unit, and $\varepsilon_u^{3/2}/\sqrt{\alpha}$ is the pump unit. After the above transformation in eq 11, eq 10 can be matched exactly with eq 3.

We set $a = 3\ \mu$m, which makes the diameter of the *main* pillars 3 μm and that for the *auxiliary* pillars 3.4 μm. The spacing between the *main* pillars becomes 6.4 μm. Such a system of micropillars is readily achieved in experiments.[59,70,71] By choosing $m = 5 \times 10^{-5} m_e$, where m_e is the free electron mass, the energy unit becomes $\varepsilon_u \approx 0.085$ meV. Fixing the energy unit also fixes all the energy scales. The topological band gap becomes around 0.12 meV, the effective potential depth for the polaritons becomes 20 meV, and the lifetime becomes 30 ps. The energy scale can be increased by choosing smaller sized micropillars and reducing a, which increases ε_u. Alternatively, by adjusting the detuning between the exciton and photon branches, the effective mass of the polaritons can be reduced, thereby increasing ε_u.

Another important parameter is the nonlinear interaction constant α. The value of α can be controlled by adjusting the exciton fraction of the polaritons. However, measuring α exactly in experiments is difficult and still an ongoing research. The measurable quantity in experiments is the blueshift $\alpha|\phi|^2$. For the above-mentioned parameters the blueshift for the low-intensity state is around 0.03 meV and that for the high-intensity state is around 0.35 meV. Such values of blueshift are routine observations in experiments.[72,73]

For the introduction of the gain at the four corners, an optical pump positioned at the corner having much higher energy from the polariton resonance can be used. The pump creates free electron−hole pairs, which relax down and form the excitonic reservoir. The density of the excitons in the excitonic reservoir acts as gain to the polaritons.[69] Alternatively, it is also possible to arrange gain using electrical pumping.[74−76]

CONCLUSION

To conclude, we have presented a new concept, where the topological phase can be induced as a memory. In particular, we show that a nonlinear system of photonic lossy resonators goes through a topological phase transition under the application of a coherent pulse. The system continues to maintain its topology, although the effect of the pulse disappears. The topological modes can show fair robustness against realistic disorder (see Supporting Information). This scheme is independent of the dimension, and similar effects can be found in 1D lattices (see Supporting Information). Our scheme is the first example where on-site Kerr nonlinearity induces higher-order topology and can be useful in triggering different functionalities of active topological photonic devices.

ASSOCIATED CONTENT

Supporting Information

The Supporting Information is available free of charge at https://pubs.acs.org/doi/10.1021/acsphotonics.2c01367.

Additional calculations including the discussion on bistability, effective tight binding model, calculation of the topological invariant, robustness of the scheme, and 1D topological memory (PDF)

Movie 1 showing the memory effect without the gain at the corner and Movie 2 showing the triggering of the amplification of the corner modes with a pulse (ZIP)

AUTHOR INFORMATION

Corresponding Authors

Subhaskar Mandal − *Division of Physics and Applied Physics, School of Physical and Mathematical Sciences, Nanyang Technological University, Singapore 637371, Singapore;* orcid.org/0000-0002-3202-9364; Email: subhaskar.mandal@ntu.edu.sg

Baile Zhang − *Division of Physics and Applied Physics, School of Physical and Mathematical Sciences, Nanyang*

https://doi.org/10.1021/acsphotonics.2c01367
ACS Photonics 2023, 10, 147−154

Technological University, Singapore 637371, Singapore; orcid.org/0000-0003-1673-5901; Email: blzhang@ntu.edu.sg

Author

Gui-Geng Liu − *Division of Physics and Applied Physics, School of Physical and Mathematical Sciences, Nanyang Technological University, Singapore 637371, Singapore*

Complete contact information is available at: https://pubs.acs.org/10.1021/acsphotonics.2c01367

Funding

This research is supported by the Singapore National Research Foundation Competitive Research Program under Grant No. NRF-CRP23-2019-0007, and the Singapore Ministry of Education Academic Research Fund Tier 3 Grant MOE2016-T3-1-006.

Notes

The authors declare no competing financial interest.

■ ACKNOWLEDGMENTS

S.M. thanks Dr. Rimi Banerjee for helpful discussions.

■ REFERENCES

(1) Wang, Z.; Chong, Y.; Joannopoulos, J. D.; Soljačić, M. Observation of unidirectional backscattering-immune topological electromagnetic states. *Nature* **2009**, *461*, 772−775.
(2) Poo, Y.; Wu, R.; Lin, Z.; Yang, Y.; Chan, C. T. Experimental Realization of Self-Guiding Unidirectional Electromagnetic Edge States. *Phys. Rev. Lett.* **2011**, *106*, 093903.
(3) Shalaev, M. I.; Walasik, W.; Tsukernik, A.; Xu, Y.; Litchinitser, N. M. Robust topologically protected transport in photonic crystals at telecommunication wavelengths. *Nat. Nanotechnol.* **2019**, *14*, 31−34.
(4) He, X. T.; Liang, E. T.; Yuan, J. J.; Qiu, H. Y.; Chen, X. D.; Zhao, F. L.; Dong, J. W. A silicon-on-insulator slab for topological valley transport. *Nat. Commun.* **2019**, *10*, 872.
(5) Yang, Y.; Yamagami, Y.; Yu, X.; Pitchappa, P.; Webber, J.; Zhang, B.; Fujita, M.; Nagatsuma, T.; Singh, R. Terahertz topological photonics for on-chip communication. *Nat. Photonics* **2020**, *14*, 446−451.
(6) Hafezi, M.; Demler, E. A.; Lukin, M. D.; Taylor, J. M. Robust optical delay lines with topological protection. *Nat. Phys.* **2011**, *7*, 907−912.
(7) Barik, S.; Karasahin, A.; Flower, C.; Cai, T.; Miyake, H.; DeGottardi, W.; Hafezi, M.; Waks, E. A topological quantum optics interface. *Science* **2018**, *359*, 666−668.
(8) Mittal, S.; Goldschmidt, E. A.; Hafezi, M. A topological source of quantum light. *Nature* **2018**, *561*, 502−506.
(9) Cheng, X.; Jouvaud, C.; Ni, X.; Mousavi, S. H.; Genack, A. Z.; Khanikaev, A. B. Robust reconfigurable electromagnetic pathways within a photonic topological insulator. *Nat. Mater.* **2016**, *15*, 542−548.
(10) St-Jean, P.; Goblot, V.; Galopin, E.; Lemaître, A.; Ozawa, T.; Le Gratiet, L.; Sagnes, I.; Bloch, J.; Amo, A. Lasing in topological edge states of a one-dimensional lattice. *Nat. Photonics* **2017**, *11*, 651−656.
(11) Bahari, B.; Ndao, A.; Vallini, F.; El Amili, A.; Fainman, Y.; Kanté, B. Nonreciprocal lasing in topological cavities of arbitrary geometries. *Science* **2017**, *358*, 636−640.
(12) Bandres, M. A.; Wittek, S.; Harari, G.; Parto, M.; Ren, J.; Segev, M.; Christodoulides, D. N.; Khajavikhan, M. Topological insulator laser: Experiments. *Science* **2018**, *359*, eaar4005.
(13) Zeng, Y.; Chattopadhyay, U.; Zhu, B.; Qiang, B.; Li, J.; Jin, Y.; Li, L.; Davies, A. G.; Linfield, E. H.; Zhang, B.; Chong, Y.; Wang, Q. J. Electrically pumped topological laser with valley edge modes. *Nature* **2020**, *578*, 246−250.
(14) Smirnova, D.; Tripathi, A.; Kruk, S.; Hwang, M.; Kim, H.; Park, H.; Kivshar, Y. Room-temperature lasing from nanophotonic topological cavities. *Light Sci. Appl.* **2020**, *9*, 127.
(15) Leykam, D.; Chong, Y. D. Edge Solitons in Nonlinear-Photonic Topological Insulators. *Phys. Rev. Lett.* **2016**, *117*, 143901.
(16) Kartashov, Y. V.; Skryabin, D. V. Modulational instability and solitary waves in polariton topological insulators. *Optica* **2016**, *3*, 1228−1236.
(17) Mukherjee, S.; Rechtsman, M. C. Observation of Floquet solitons in a topological bandgap. *Science* **2020**, *368*, 856−859.
(18) Mukherjee, S.; Rechtsman, M. C. Observation of Unidirectional Solitonlike Edge States in Nonlinear Floquet Topological Insulators. *Phys. Rev. X* **2021**, *11*, 041057.
(19) Pernet, N.; et al. Gap solitons in a one-dimensional driven-dissipative topological lattice. *Nat. Phys.* **2022**, *18*, 678−684.
(20) Kruk, S.; Poddubny, A.; Smirnova, D.; Wang, L.; Slobozhanyuk, A.; Shorokhov, A.; Kravchenko, I.; Luther-Davies, B.; Kivshar, Y. Nonlinear light generation in topological nanostructures. *Nat. Nanotechnol.* **2019**, *14*, 126−130.
(21) Wang, Y.; Lang, L. J.; Lee, C. H.; Zhang, B.; Chong, Y. D. Topologically enhanced harmonic generation in a nonlinear transmission line metamaterial. *Nat. Commun.* **2019**, *10*, 1102.
(22) Bardyn, C. E.; Karzig, T.; Refael, G.; Liew, T. C. H. Chiral Bogoliubov excitations in nonlinear bosonic systems. *Phys. Rev. B* **2016**, *93*, 020502.
(23) Hadad, Y.; Soric, J. C.; Khanikaev, A. B.; Alù, A. Self-induced topological protection in nonlinear circuit arrays. *Nat. Electron.* **2018**, *1*, 178.
(24) Zhou, X.; Wang, Y.; Leykam, D.; Chong, Y. D. Optical isolation with nonlinear topological photonics. *New J. Phys.* **2017**, *19*, 095002.
(25) Mandal, S.; Ge, R.; Liew, T. C. H. Antichiral edge states in an exciton polariton strip. *Phys. Rev. B* **2019**, *99*, 115423.
(26) Zangeneh-Nejad, F.; Fleury, R. Nonlinear Second-Order Topological Insulators. *Phys. Rev. Lett.* **2019**, *123*, 053902.
(27) Maczewsky, L. J.; Heinrich, M.; Kremer, M.; Ivanov, S. K.; Ehrhardt, M.; Martinez, F.; Kartashov, Y. V.; Konotop, V. V.; Torner, L.; Bauer, D.; Szameit, A. Nonlinearity-induced photonic topological insulator. *Science* **2020**, *370*, 701−704.
(28) Lumer, Y.; Plotnik, Y.; Rechtsman, M. C.; Segev, M. Self-Localized States in Photonic Topological Insulators. *Phys. Rev. Lett.* **2013**, *111*, 243905.
(29) Kartashov, Y. V.; Skryabin, D. V. Bistable Topological Insulator with Exciton-Polaritons. *Phys. Rev. Lett.* **2017**, *119*, 253904.
(30) Banerjee, R.; Mandal, S.; Liew, T. C. H. Coupling between Exciton-Polariton Corner Modes through Edge States. *Phys. Rev. Lett.* **2020**, *124*, 063901.
(31) Xia, S.; Kaltsas, D.; Song, D.; Komis, I.; Xu, J.; Szameit, A.; Buljan, H.; Makris, K. G.; Chen, Z. Nonlinear tuning of PT symmetry and non-Hermitian topological states. *Science* **2021**, *372*, 72−76.
(32) Kirsch, M. S.; Zhang, Y.; Kremer, M.; Maczewsky, L. J.; Ivanov, S. K.; Kartashov, Y. V.; Torner, L.; Bauer, D.; Szameit, A.; Heinrich, M. Nonlinear second-order photonic topological insulators. *Nat. Phys.* **2021**, *17*, 995−1000.
(33) Ezawa, M. Nonlinearity-induced transition in the nonlinear Su-Schrieffer-Heeger model and a nonlinear higher-order topological system. *Phys. Rev. B* **2021**, *104*, 235420.
(34) Smirnova, D.; Leykam, D.; Chong, Y.; Kivshar, Y. Nonlinear topological photonics. *Appl. Phys. Rev.* **2020**, *7*, 021306.
(35) Yu, S.; Piao, X.; Park, N. Neuromorphic Functions of Light in Parity-Time-Symmetric Systems. *Advanced Science* **2019**, *6*, 1900771.
(36) Xie, B. Y.; Wang, H. F.; Wang, H. X.; Zhu, X. Y.; Jiang, J. H.; Lu, M. H.; Chen, Y. F. Second-order photonic topological insulator with corner states. *Phys. Rev. B* **2018**, *98*, 205147.
(37) Moreno, I.; Davis, J. A.; Hernandez, T. M.; Cottrell, D. M.; Sand, D. Complete polarization control of light from a liquid crystal spatial light modulator. *Opt. Express* **2012**, *20*, 364−376.
(38) Töpfer, J. D.; Chatzopoulos, I.; Sigurdsson, H.; Cookson, T.; Rubo, Y. G.; Lagoudakis, P. G. Engineering spatial coherence in lattices of polariton condensates. *Optica* **2021**, *8*, 106−113.

(39) Dormand, J. R.; Prince, P. J. A family of embedded Runge-Kutta formulae. *J. Comput. Appl. Math.* **1980**, *6*, 19−26.
(40) Pitaevskii, L. P., Stringari, S.*Bose Einstein Condensation*; Oxford University Press: Oxford, England, 2003.
(41) Benalcazar, W. A.; Bernevig, B. A.; Hughes, T. L. Quantized electric multipole insulators. *Science* **2017**, *357*, 61−66.
(42) Liu, T.; Zhang, Y.-R.; Ai, Q.; Gong, Z.; Kawabata, K.; Ueda, M.; Nori, F. Second-Order Topological Phases in Non-Hermitian Systems. *Phys. Rev. Lett.* **2019**, *122*, 076801.
(43) Hu, Z.; Bongiovanni, D.; Jukić, D.; Jajtić, E.; Xia, S.; Song, D.; Xu, J.; Morandotti, R.; Buljan, H.; Chen, Z. Nonlinear control of photonic higher-order topological bound states in the continuum. *Light Sci. Appl.* **2021**, *10*, 164.
(44) Cheng, D.; Peng, B.; Xiao, M.; Chen, X.; Yuan, L.; Fan, S. Truncation-dependent PT phase transition for the edge states of a two-dimensional non-Hermitian system. *Phys. Rev. B* **2022**, *105*, L201105.
(45) Benalcazar, W. A.; Bernevig, B. A.; Hughes, T. L. Electric multipole moments, topological multipole moment pumping, and chiral hinge states in crystalline insulators. *Phys. Rev. B* **2017**, *96*, 245115.
(46) Luo, X.-W.; Zhang, C. Higher-Order Topological Corner States Induced by Gain and Loss. *Phys. Rev. Lett.* **2019**, *123*, 073601.
(47) Zograf, G.; Koshelev, K.; Zalogina, A.; Korolev, V.; Hollinger, R.; Choi, D.-Y.; Zuerch, M.; Spielmann, C.; Luther-Davies, B.; Kartashov, D.; Makarov, S. V.; Kruk, S. S.; Kivshar, Y. High-Harmonic Generation from Resonant Dielectric Metasurfaces Empowered by Bound States in the Continuum. *ACS Photonics* **2022**, *9*, 567−574.
(48) Smirnova, D.; Kruk, S.; Leykam, D.; Melik-Gaykazyan, E.; Choi, D.-Y.; Kivshar, Y. Third-Harmonic Generation in Photonic Topological Metasurfaces. *Phys. Rev. Lett.* **2019**, *123*, 103901.
(49) Choi, S.; Kim, J.; Kwak, J.; Park, N.; Yu, S. Topologically Protected All-Optical Memory. *Adv. Electron. Mater.* **2022**, *8*, 2200579.
(50) Yu, S.; Piao, X.; Park, N. Topologically protected optical signal processing using parity-time-symmetric oscillation quenching. *Nanophotonics* **2021**, *10*, 2883−2891.
(51) Khomeriki, R.; Leon, J. Light Detectors Bistable Nonlinear Waveguide Arrays. *Phys. Rev. Lett.* **2005**, *94*, 243902.
(52) Solntsev, A. S.; et al. Generation of Nonclassical Biphoton States through Cascaded Quantum Walks on a Nonlinear Chip. *Phys. Rev. X* **2014**, *4*, 031007.
(53) Kruse, R.; Katzschmann, F.; Christ, A.; Schreiber, A.; Wilhelm, S.; Laiho, K.; Gábris, A.; Hamilton, C. S.; Jex, I.; Silberhorn, C. Spatio-spectral characteristics of parametric down-conversion in waveguide arrays. *New J. Phys.* **2013**, *15*, 083046.
(54) Peano, V.; Houde, M.; Brendel, C.; Marquardt, F.; Clerk, A. A. Topological phase transitions and chiral inelastic transport induced by the squeezing of light. *Nat. Commun.* **2016**, *7*, 10779.
(55) Yang, Y.; Zuo, Z.; Cao, D. Biphoton topology in a quadratic nonlinear waveguide array under the Su-Schrieffer-Heeger model. *Phys. Rev. A* **2021**, *104*, 043710.
(56) Doyle, C.; Zhang, W.-W.; Wang, M.; Bell, B. A.; Bartlett, S. D.; Blanco-Redondo, A. Biphoton entanglement of topologically distinct modes. *Phys. Rev. A* **2022**, *105*, 023513.
(57) Bardyn, C.-E.; Karzig, T.; Refael, G.; Liew, T. C. H. Topological polaritons and excitons in garden-variety systems. *Phys. Rev. B* **2015**, *91*, 161413.
(58) Nalitov, A. V.; Solnyshkov, D. D.; Malpuech, G. Polariton Z Topological Insulator. *Phys. Rev. Lett.* **2015**, *114*, 116401.
(59) Klembt, S.; Harder, T. H.; Egorov, O. A.; Winkler, K.; Ge, R.; Bandres, M. A.; Emmerling, M.; Worschech, L.; Liew, T. C. H.; Segev, M.; Schneider, C.; Höfling, S. Exciton-polariton topological insulator. *Nature* **2018**, *562*, 552−556.
(60) Banerjee, R.; Liew, T. C. H.; Kyriienko, O. Realization of Hofstadter's butterfly and a one-way edge mode in a polaritonic system. *Phys. Rev. B* **2018**, *98*, 075412.
(61) Kartashov, Y. V.; Skryabin, D. V. Two-Dimensional Topological Polariton Laser. *Phys. Rev. Lett.* **2019**, *122*, 083902.
(62) Mandal, S.; Banerjee, R.; Ostrovskaya, E. A.; Liew, T. C. H. Nonreciprocal Transport of Exciton Polaritons in a Non-Hermitian Chain. *Phys. Rev. Lett.* **2020**, *125*, 123902.
(63) Mandal, S.; Banerjee, R.; Liew, T. C. H. From the Topological Spin-Hall Effect to the Non-Hermitian Skin Effect in an Elliptical Micropillar Chain. *ACS Photonics* **2022**, *9*, 527−539.
(64) Harder, T. H.; Sun, M.; Egorov, O. A.; Vakulchyk, I.; Beierlein, J.; Gagel, P.; Emmerling, M.; Schneider, C.; Peschel, U.; Savenko, I. G.; Klembt, S.; Höfling, S. Coherent Topological Polariton Laser. *ACS Photonics* **2021**, *8*, 1377−1384.
(65) Baas, A.; Karr, J. P.; Eleuch, H.; Giacobino, E. Optical bistability in semiconductor microcavities. *Phys. Rev. A* **2004**, *69*, 023809.
(66) Paraïso, T. K.; Wouters, M.; Léger, Y.; Morier-Genoud, F.; Deveaud-Plédran, B. Multistability of a coherent spin ensemble in a semiconductor microcavity. *Nat. Mater.* **2010**, *9*, 655−660.
(67) Banerjee, R.; Liew, T. C. H. Artificial life in an exciton-polariton lattice. *New J. Phys.* **2020**, *22*, 103062.
(68) Utsunomiya, S.; Tian, L.; Roumpos, G.; Lai, C. W.; Kumada, N.; Fujisawa, T.; Kuwata-Gonokami, M.; Löffler, A.; Höfling, S.; Forchel, A.; Yamamoto, Y. Observation of Bogoliubov excitations in exciton-polariton condensates. *Nat. Phys.* **2008**, *4*, 700−705.
(69) Carusotto, I.; Ciuti, C. Quantum fluids of light. *Rev. Mod. Phys.* **2013**, *85*, 299.
(70) Harder, T. H.; Egorov, O. A.; Beierlein, J.; Gagel, P.; Michl, J.; Emmerling, M.; Schneider, C.; Peschel, U.; Höfling, S.; Klembt, S. Exciton-polaritons in flatland: Controlling flatband properties in a Lieb lattice. *Phys. Rev. B* **2020**, *102*, 121302.
(71) Dusel, M.; Betzold, S.; Egorov, O. A.; Klembt, S.; Ohmer, J.; Fischer, U.; Höfling, S.; Schneider, C. Room temperature organic exciton-polariton condensate in a lattice. *Nat. Commun.* **2020**, *11*, 2863.
(72) Sun, Y.; Yoon, Y.; Steger, M.; Liu, G.; Pfeiffer, L. N.; West, K.; Snoke, D.; Nelson, K. A. Direct measurement of polariton−polariton interaction strength. *Nat. Phys.* **2017**, *13*, 870−875.
(73) Estrecho, E.; Gao, T.; Bobrovska, N.; Comber-Todd, D.; Fraser, M. D.; Steger, M.; West, K.; Pfeiffer, L. N.; Levinsen, J.; Parish, M. M.; Liew, T. C. H.; Matuszewski, M.; Snoke, D. W.; Truscott, A. G.; Ostrovskaya, E. A. Direct measurement of polariton-polariton interaction strength in the Thomas-Fermi regime of exciton-polariton condensation. *Phys. Rev. B* **2019**, *100*, 035306.
(74) Schneider, C.; et al. An electrically pumped polariton laser. *Nature* **2013**, *497*, 348−352.
(75) Klaas, M.; Mandal, S.; Liew, T. C. H.; Amthor, M.; Klembt, S.; Worschech, L.; Schneider, C.; Höfling, S. Optical probing of the Coulomb interactions of an electrically pumped polariton condensate. *Appl. Phys. Lett.* **2017**, *110*, 151103.
(76) Gagel, P.; Harder, T. H.; Betzold, S.; Egorov, O. A.; Beierlein, J.; Suchomel, H.; Emmerling, M.; Wolf, A.; Peschel, U.; Höfling, S.; Schneider, C.; Klembt, S. Electro-optical Switching of a Topological Polariton Laser. *ACS Photonics* **2022**, *9*, 405−412.

https://doi.org/10.1021/acsphotonics.2c01367
ACS Photonics 2023, 10, 147−154